Electrochemical and corrosion behaviour of sputtered TiNi shape memory films

K. Li[1,2,*], X. Huang[3,*], Z.S. Zhao[4], Y. Li[1,] and Y.Q. Fu[2,**]**
[1]School of Materials Science and Engineering, Beihang University, Beijing, 100191, China
[2]Department of Physics and Electrical Engineering, Faculty of School of Engineering and Environment, Northumbria University, Newcastle Upon Tyne, NE1 8ST, UK.
[3]College of Materials Science and Engineering, Taiyuan University of Technology, Shanxi, China

*The authors have equal contribution to the paper.

** Corrsponding authors: Prof. Yan Li: liyan@buaa.edu.cn; Dr. Richard Yongqing Fu, richard.fu@northumbria.ac.uk

Abstract Electrochemical and corrosion behaviors of TiNi-based shape memory thin films were explored using electrochemical impedance spectroscopy (EIS) and polarization methods in phosphate buffered saline (PBS) solutions at 37°C. Compared with those of electro-polished and passivated bulk NiTi shape memory alloys, the break-down potentials of the sputter-deposited amorphous TiNi films were much higher. After crystallization, the break-down potentials of the TiNi films were comparable with that of the bulk NiTi shape memory alloy. Additionally, variation of composition of the TiNi films showed little influence on their corrosion behaviour. The EIS data were fitted using a parallel resistance-capacitance circuit associated with passive oxide layer on the tested samples. The thickness of the oxide layer for the TiNi thin films was found much thinner than that of bulk NiTi shape memory alloy. During electrochemical testing, the oxide thickness of the bulk alloy reached its maximum at a voltage of 0.6~0.8 V, whereas those of TiNi films were increased continuously up to a voltage of 1.2 V.

Keywords: thin film, NiTi shape memory alloy, corrosion, electrochemical impedance spectroscopy, oxide thickness

1. Introduction

There is a significantly increased interest for shape memory materials (SMAs)in the past decades [1-10]. Among the different types of SMAs, TiNi shape memory alloy films have been extensively explored recently since they can generate larger stress/strain compared to other candidates used in micro-electro-mechanical systems [4-10] due to their shape memory effect and superelasticity. Magnetron sputtering has been regarded as one of the best ways to deposit TiNi films [5,8]. When the films are deposited at an ambient temperature, they are normally amorphous and post-annealing crystallization is required to introduce shape memory and superelastic properties. It has been documented that the properties of TiNi films are comparable with those of bulk NiTi shape memory alloys (or commonly known as nitinol), if not better [4-10]. Recently, great effort has been made to apply TiNi films into biomedical devices, for example, microgripper and implant stents [5,11].

Nitinol is the most conventional shape memory materials used for medical and industrial applications [12,13]. For implant medical devices, the high content of Ni in the nitinol has always been a concern as Ni ions are known to be allergic, toxic and carcinogenic, even though the nitinol has been verified as one of good biocompatible materials [14]. The good biocompatibility of the nitinol relies on the spontaneous formation of a protective TiO_2 layer on the alloy surface [15]. In addition, the TiO_2 layer can be treated as an elastic and hard layer atop the nitinol thin film, hence there are reversible trenches, i.e., elastic buckling, during thermomechanical cycling [16]. Therefore, surface treatment has been commonly applied for the nitinol in order to improve its corrosion resistance and decrease the Ni ion leaching [15,17-19]. Currently, passivation followed by electro-chemical polishing has been developed as a standard method for improving the corrosion and fatigue resistance of the bulk nitinol [20,21].

Microstructure and properties of surface passivation layer are critical for the corrosion resistance of the nitinol [22]. It was reported that corrosion resistance of amorphous alloys was better than that of its crystalline counterpart [22,23]. However, it is complicated to fabricate bulk amorphous NiTi alloys in order to improve its corrosion resistance, where severe plastic deformation might be necessary [24]. Moreover, the bulk nitinol will lose its shape memory and superelasticity in the amorphous conditions. On the other hand, homogeneous and dense amorphous TiNi films can be readily sputter–deposited onto the substrate, such as nitinol at an ambient temperature, thus the corrosion resistance could be improved significantly [5,8,25]. However, there is no systematic report on the corrosion performance of the sputtered TiNi films.

Electrochemical impedance spectroscopy (EIS) has been widely used to study the corrosion resistance of materials and associated potential inhibitors, fuel cells, biosensors, batteries, nanoparticles, and passivation layers, etc, and a number of studies have employed the EIS to examine passivation behavior of Ti and its alloys in simulated physiological solutions [26-28]. It was found that the passivated TiO_2 layer on the nitinol can be classified as an N-type semiconductor, and the thickness of oxide layer was increases with potential [27]. However, for the sputtered TiNi films, there are only few reports on polarization behaviors in the simulated body fluids [11]. Therefore, in the present study, corrosion and electrochemical behaviors of the sputtered TiNi films are systematically investigated using potentio-dynamic polarization and EIS methods.

2. Experimental Procedures

Amorphous near equi-atomic TiNi films of 1 μm thick were sputter-deposited onto Si_3N_x-coated silicon wafer, and the detail deposition parameters have previously been

reported [9]. The base pressure was 2.0×10^{-7} Torr and the argon pressure was 2.4 mTorr during the deposition. Targets of TiNi and Ti, both with a size of 100 mm diameters, and DC plasma powers of 400 W and 70 W, were co-sputtered at ambient temperature onto the silicon substrates, which generated a deposition rate of 0.76 nm/sec for the TiNi film. The composition of TiNi films was determined using an electron microprobe. The crystallization of the as-deposited TiNi films was conducted using an RF heating system equipped with a high vacuum (base vacuum of 5×10^{-6}Torr) at 650°C for 5 minutes.

Cyclic potentio-dynamic polarization method was used to characterize the corrosion resistance of the TiNi film and nitinol bulk reference. The corrosion resistance of the TiNi/Si_3N_x/Si component was conducted in a phosphate buffered saline (PBS) solution at 37°C following ASTM Standard F2129-08 [29]. The PBS solution was de-aerated using pure N_2 gas for 30 minutes, and the N_2 gas was introduced into the PBS solution during the measurement. A saturated calomel reference electrode (SCE) was used, and the scan rate was 1 mV/second.

EIS tests of TiNi-based thin films were conducted at DC potentials from E_{corr} to 1.2 V (SCE) with a step of 0.2 V. During measurement, an AC voltage of 10 mV was potentio-statically imposed on the DC potential at frequencies between 0.01 Hz and 10 kHz. The E_{corr} was monitored for 60 minutes after the sample was immersed into the PBS solution at 37°C. When the potential was step-wisely increased to the subsequent value, the current was allowed to stabilize for 15 minutes before the measurement was performed.

3. Results and Discussion

3.1 Cyclic polarization behaviors of TiNi thin films

Typical cyclic polarization curves for the as-sputtered amorphous Ti-51at.%Ni and Ti-48at.%Ni thin films in the PBS solutions are presented in Figure 1, and the results of a conventional electropolished bulk Ti-50.8at%Ni wires were plotted for a comparison.

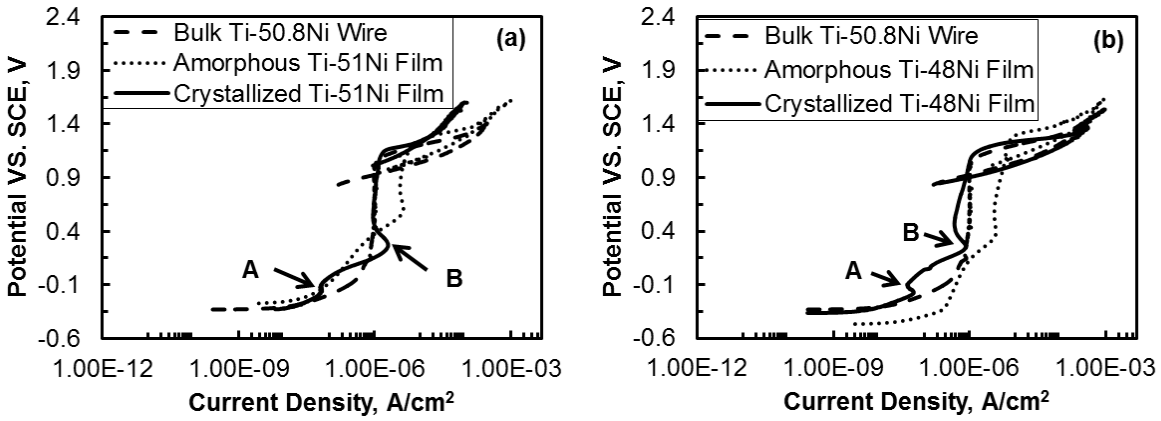

Figure 1. The cyclic polarization curves of sputtered (a) Ti-51at.%Ni and (b) Ti-48at.%Ni shape memory thin films. The electropolished Ti-50.8at.%Ni wire is also plotted for a comparison.

The obtained potential of amorphous TiNi film is comparable with that of bulk nitinol wire, in the range of -360~-460 mV. However, the anodic behaviors of the amorphous TiNi films are slightly different from those of bulk nitinol wire. For the as-deposited amorphous TiNi films, the anodic curves form a concave-shape between Points A and B at the beginning of anodic polarization curves, i.e., the two arrows indicated in Figure 1. When the applied potential is above the Point B, the current density keeps almost a constant with increasing potential, and this current density is termed as $i_{passivation}$ in the present study for an easy description. Moreover, the value of $i_{passivation}$ decreases slightly at the Point B, implying that the as-sputtered amorphous Ti-51at.%Ni and Ti-48at.%Ni thin films exhibit a good capability of re-passivation. However, the concave shape does not exist in the bulk nitinol wires at the beginning segment of anodic polarization curve; andwhen the current density reaches the $i_{passivation}$, it remains almost a constant with further increasing applied potential. The

concave-shape curve at the beginning of anodic polarization results in a higher $i_{passivation}$ for the as-sputtered amorphous TiNi films. Interestingly, the Ti/Ni ratio has insignificant effect on the measured $i_{passivation}$ values of the amorphous TiNi films as shown in Figure 1.

The crystallization also affects the corrosion behavior of the sputtered TiNi films as well. As shown in Figure 1, the value of $i_{passivation}$ of crystallized TiNi film is much smaller than the counterparts of amorphous ones, but is still comparable to that of bulk nitinol. Additionally, this crystallization effect is not significantly influenced by Ti/Ni ratio, as shown in Figure 1. Moreover, the crystallized TiNi films exhibit an apparently good re-passivation capability, based on the changes of Point B indicated in the Figure 1. On the contrary, the re-passivation behavior has not been observed in the bulk nitinol wires.

From Figure 1, the break-down potential of the amorphous TiNi film is higher than that of bulk nitinol wires. This observation is consistent with literature that the corrosion resistance of the amorphous materials is better than that of the crystalline counterparts [22,23]. The higher corrosion resistance of the amorphous TiNi films compared to that of the bulk nitinol might be related to the less contents of inclusions and small-grain structures in the TiNi films, since the pitting is usually initiated at these defects, including non-metallic inclusions, grain boundaries and precipitates [30]. Additionally, the corrosion resistance is independent of the Ti/Ni ratios for the amorphous TiNi thin films as shown in Figure 1. After crystallization, the break-down potential of the sputtered TiNi films decreases, but is still in the similar level as that of bulk nitinol wires. It is worthwhile to point out that the measured breakdown potential of sputtered TiNi films is around 1 V, which is in the data range of oxidation of water, rather than the localized breakdown of surface oxide layer [27]. The absence of pitting was further confirmed through examining the samples after cyclic potentio-dynamic tests. In

brief, the corrosion resistance of as-sputtered TiNi films is superior to that of bulk nitinol counterparts.

3.2 Electrochemical impedance spectroscopy of TiNi thin films

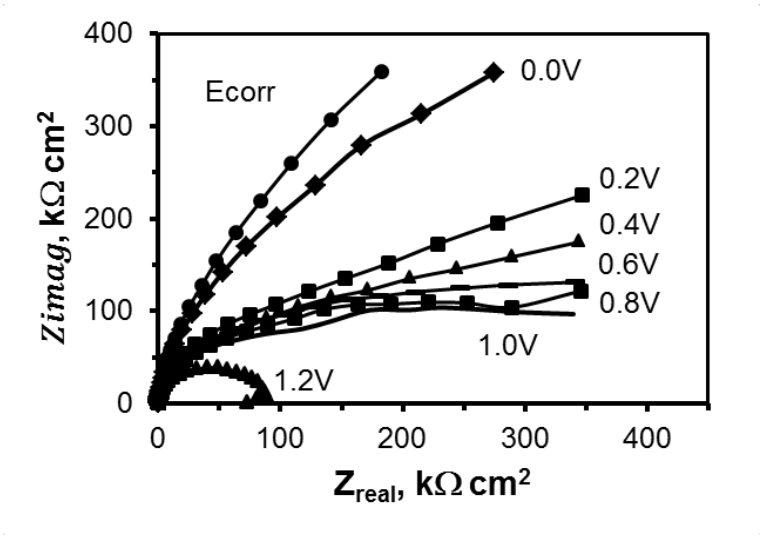

Figure 2. The complex plane plots of amorphous Ti-48at.%Ni TiNi films in PBS solution at 37°C. Frequency range: 10 mHz to 10 kHz.

The surface oxide layer of sputtered TiNi films in the PBS solutions at 37°C were characterized using the EIS, and figure 2 presents the corresponding Nyquist plots, or complex plane plots of the real (Z_{real}) and imaginary (Z_{imag}) impedance components of amorphous Ti-48at.%Ni films. For an easy comparison, all the data have been normalized to the sample surface area in the present study. The impedance exhibits a systematic change with increasing the applied potential up to 1.0 V. When the potential was step-increased from 0.0 V to 0.2 V, the impedance exhibits a relatively large decrement at a lower frequency. With the potential further increased up to 1.0 V, the impedance decrement is relatively small. This observation might be related to the concave-shape curve at the beginning anodic polarization as shown in Figure 1. When the potential is further increased to 1.2 V, the

impedance components decrease significantly, forming a semi-circle shape. This observation is attributed to the oxidation evolution of the solution, rather than the breakdown of surface oxide layer [27].

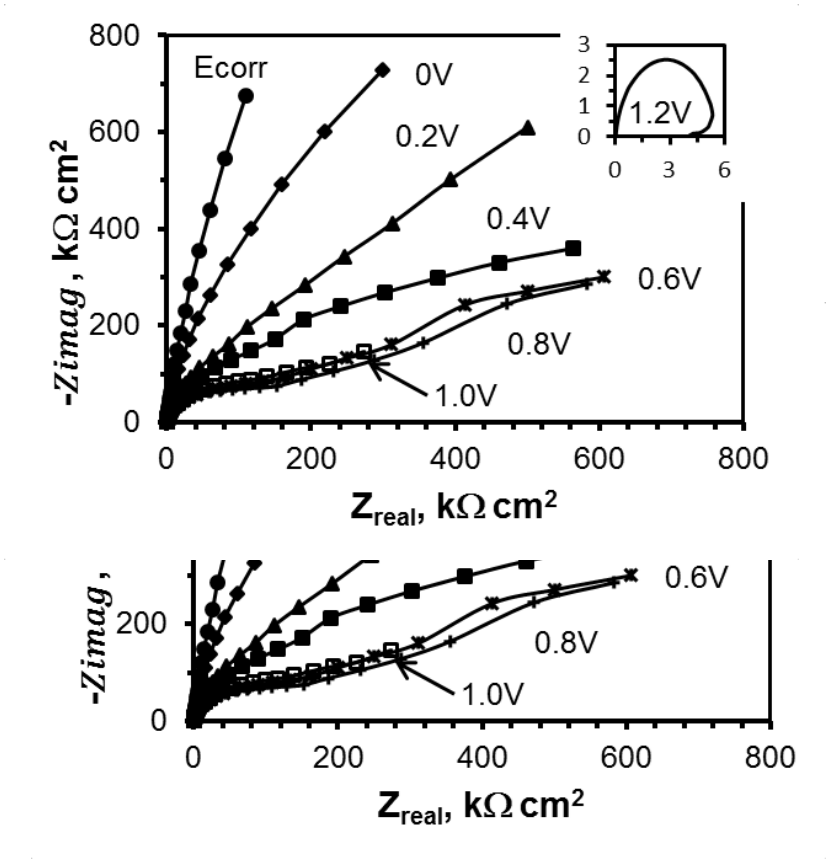

Figure 3. The complex plane plots of electropolished bulk nitinol wires in PBS solution at 37°C. Frequency range: 10 mHz to 10 kHz.

For an easy comparison, the complex plane plots of electro-polished bulk nitinol wires are presented in Figure 3, which is consistent with those in the literature [27]. The impedance evolution behavior is comparable for the amorphous TiNi films and the bulk nitinol wires.

Figure 4. Bode plots of amorphous Ti-48at.%Ni TiNi films in PBS solution at 37°C. For clarity, data are not shown for all potentials.

Figure 5. Bode plots of electropolished bulk nitinol wires in PBS solution at 37°C. For clarity, data are not shown for all potentials.

The corresponding Bode plots of amorphous Ti-48at. %Ni films and bulk nitinol wires are presented in Figures 4 and 5, respectively. A systematic increment of impedance magnitude ($|Z|$) was observed with increasing potential. The effect of potential is clearly exhibited in the phase shift angle (θ), especially at a low frequency. For amorphous Ti-48at. %Ni films, the phase shift angle θ was close to 90° over a wide frequency range when the potential was

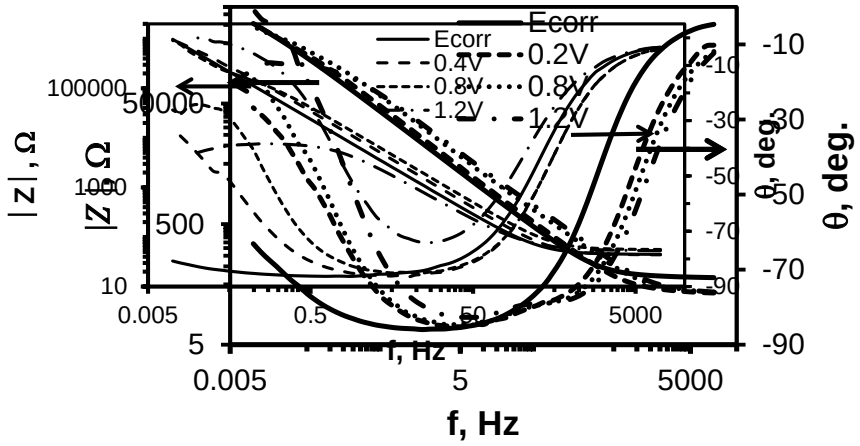

increased up to 1.2 V, indicating a near-capacitive behavior of the surface. The impedance magnitude ($log|Z|$) plots are linear in this frequency range with slopes of almost -1. However, the maximum phase shift angle θ of the bulk nitinol wires was only about 74° when the potential was increased up to 1.2 V, indicating that the near-capacitive behavior of the surface was broken, which is consistent with those in literature [27].

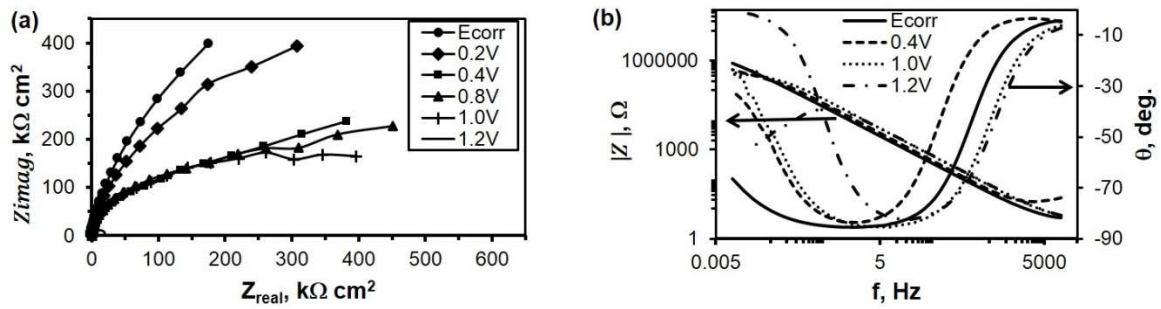

Figure 6. (a) Complex plane plots, and (b) Bode plots of amorphous Ti-51at.%Ni TiNi films in PBS solution at 37°C. For clarity, data are not shown for all potentials.

Figure 6 shows the EIS results of amorphous Ti-51at.%Ni thin films in the PBS solution at 37°C, including the complex plane plots of the real (Z_{real}) and imaginary (Z_{imag}) impedance components (Figure 6a) and Bode plots (Figure 6b). They are similar to those of the amorphous Ti-48at.%Ni thin films as shown in Figures 2 and 4. There is a significant decrease of the impedance component when the potential was increased from 0.2 to 0.4 V, while that of Ti-48at.%Ni thin films was between 0 and 0.2V (Figure 2). Re-examining Figure 1, the turning point of Ti-51at.%Ni thin films is a little higher than that of Ti-48at.%Ni thin films (i.e., Point B in Figure 1). The two phenomenon might be correlated, and further explore is required.

Crystallization affects the impedance components as well. Figures 7 and 8 present the EIS results of crystallized Ti-48at.%Ni and Ti-51at.%Ni thin films, respectively, in PBS solution at 37°C, including the complex plane plots of the real (Z_{real}) and imaginary (Z_{imag}) impedance components (Figure 7a and 8a) and Bode plots (Figure 7b and 8b).

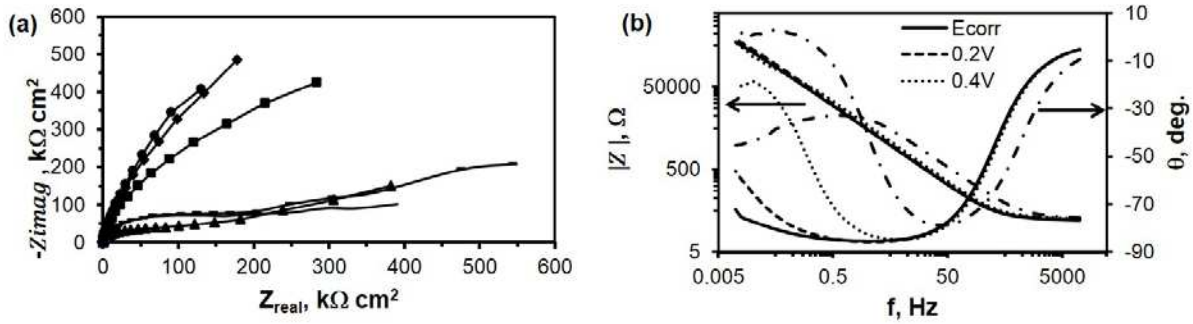

Figure 7. (a) Complex plane plots, and (b) Bode plots of crystallized Ti-48at.%Ni TiNi films in PBS solution at 37°C. For clarity, data are not shown for all potentials.

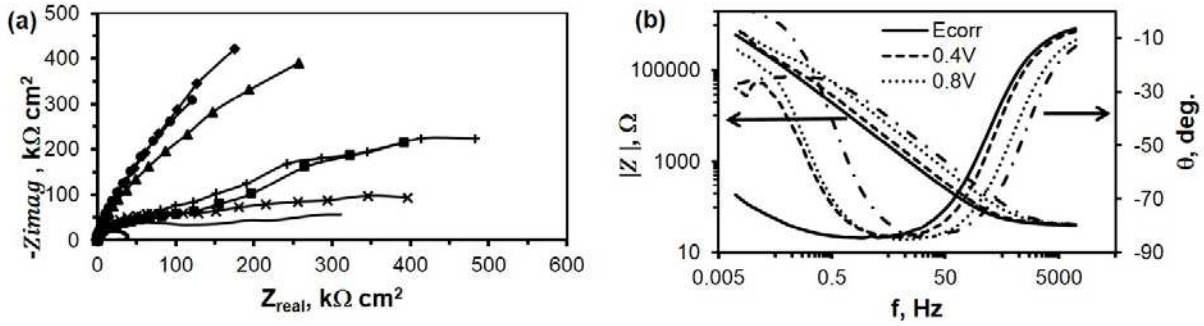

Figure 8. (a) Complex plane plots, and (b) Bode plots of crystallized Ti-51at.%Ni TiNi films in PBS solution at 37°C. For clarity, data are not shown for all potentials.

After crystallization, the impedance components of both the films have a relatively large decrement between 0.2 and 0.4 V at a low frequency. This might be related to the re-passivation behavior of sputtered films, as Point B indicating in Figure 1. Compared to those of the bulk nitinol wires, the maximum phase shift angles θ of sputtered films are much larger when the applied potential is 1.2V, implying that the corrosion resistance of sputtered films is superior to that of bulk counterparts in the PBS.

The near capacitive behavior implies that the impedance components can be represented using a simple equivalent circuit as shown in Figure 9. In literature, complex equivalent circuit was also explored to simulate the impedance data: for example, the impedance data of Ti in a physiologic solution was analyzed using an equivalent circuit that consisted of a series

resistance and a parallel combination of an interfacial capacitance and a polarization resistance [31].

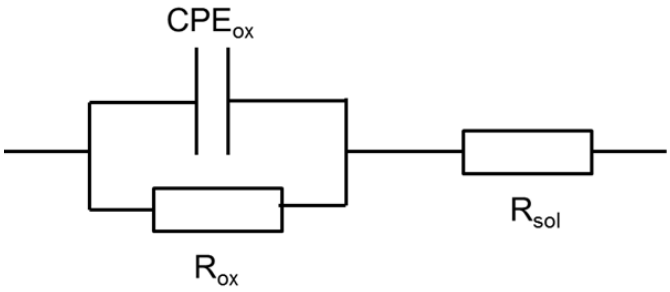

Figure 9. Equivalent circuits of TiNi films in PBS solution at 37°C.

In this case, it is assumed that the series resistance is associated with the solution and should therefore exhibit ohmic behavior. However, it was found that the series resistance varied with potential to some extent [31]. On the contrary, the polarization resistance showed little dependence on potential, which is contrary to the expected behavior [27]. Therefore, the RC-type circuit was selected in the present study, which consisted of the ohmic resistance of the solution (R_{sol}), the resistance of the passive oxide film (R_{ox}), and a constant phase element (*CPE*) associated with the oxide films. The constant phase element was used in place of a capacitance (C_{ox}) to account the non-ideal capacitive behavior of the oxide. The impedance associated with a *CPE* is given by: [27]

$$Z_{CPE} = \frac{1}{Y_0(j\omega)^{\alpha}} \quad (1)$$

where Y_0 is the constant-phase-element parameter, $j = \sqrt{-1}$, ω is the angular frequency ($\omega=2\pi f$), and α is equal to 1 for a deal capacitor. Values of R_{sol}, R_{ox}, Y_0, and α can be obtained using a nonlinear least squares curve fitting procedure. The values of α for both amorphous and crystallized TiNi films were found to be between 0.94 and 0.97. Accordingly, Y_0 can be taken as the value of C_{ox} since α is close to 1 [27,28].

The thickness of the surface oxide layer, d_{ox}, can be calculated from the values of C_{ox},

$$d_{ox} = \frac{\varepsilon\varepsilon_0}{C_{ox}} \quad (2)$$

where ε is the dielectric constant of the oxide and ε_0 is the permittivity of free space (8.854×10^{-12} F/m) [32]. The surface oxide is mainly TiO_2 for TiNi shape memory alloys [33]. The dielectric constant ε for the polycrystalline rutile was taken as 100 in the present study [27]. The calculated oxide thickness evolution with applied DC potential is presented in Figure 10, where the oxide thickness increases with the potential. This observation is consistent with the behavior of nitinol in PBS and simulated human physiological solutions

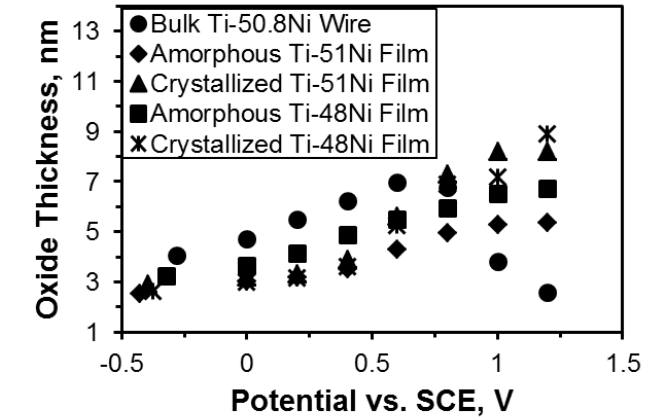

[27].

Figure 10. Comparison of calculated oxide thickness of amorphous (a) and crystallized (b) Ti-51at.%Ni and Ti-48at.%Ni shape memory thin films. The oxide thickness of electropolished bulk Ti-50.8at.%Ni wires is also plotted for comparison.

The surface oxide of Ti alloys continually increases in the PBS solution has been measured using polarization impedance spectroscopy and electrochemical atomic force microscopy [34]. The calculated oxide thickness d_{ox} of the TiNi thin films at E_{corr} is around 2.5~3.0 nm, regardless of crystallized film or amorphous films. These values are slightly lower than those of the bulk nitinol wire of about 4.0 nm [27]. For the bulk nitinol, the oxide thickness reaches

its maximum at around 0.6~0.8 V, and then decreases with further increasing DC potential. However, the oxide thickness of the TiNi films continues to increase until 1.2 V for both the crystallized and amorphous films. The curves of Figure 10 for the sputtered TiNi films can be generally divided into three segments. For the amorphous TiNi films, the slope is low between E_{corr} and 0~0.2V, however, the oxide thickness increases significantly between 0.2 and 0.8 V, and then decreases again with further increasing potential. For the crystallized counterparts, the initial low slope can reach to 0.2~0.4 V from E_{corr}, after which it has a similar trend with the amorphous counterparts. It is normally accepted that oxygen evolution starts when the applied voltage is above 0.8 V, and the oxygen evolution, in turn, affects the corrosion behavior of tested samples in PBS solution [27]. For bulk nitinol, the turning point in Figure 10 is related to the oxygen evolution in the solution. However, the oxide thickness of sputtered TiNi films continually increases even as the applied voltage is above 0.8 V, implying that the TiNi films have a better anti-oxidized capability. This observation is consistent with those from potentio-dynamic polarization scan, as shown in Figure 1.

Results showed that the corrosion resistance of the TiNi films is better than that of bulk nitinol wires. This observation provides information for the potential applications of TiNi films into corrosion resistance application, i.e., a layer of amorphous TiNi films can be deposited onto nitinol medical devices to improve it corrosion resistance. In this case, the functional properties such as shape memory or superelasticity are controlled by the bulk nitinol, and the amorphous TiNi films (here composition of Ti/Ni is not critical) will show good corrosion resistance.

4. Summary

The corrosion resistance of TiNi films was investigated using polarization and EIS methods, and the results were compared with those from the commercial electro-polished bulk nitinol wires. It was found that the corrosion resistance of TiNi films, whether in a crystallized or amorphous states, is better than that of bulk nitinol wires. Additionally, the corrosion resistance of TiNi films is insensitive to the film compositions (mainly the Ni/Ti ratio). At a value of E_{corr}, the oxide thickness of TiNi films is thinner than that of bulk nitinol, however, it increases with potential up to 1.2 V, whereas that of bulk nitinol reached its maximum at around 0.6~0.8 V.

Acknowledgements

The authors acknowledge support from Royal Academy of Engineering-Research Exchange with China and India and the National Natural Science Foundation of China (NSFC, No. 51171009). Some of the samples used in the present study were provided by Dr. A.G. Ramirez.

References

[1] X G Guo, L W Liu, Y J Liu, B Zhou and J S Leng 2014 Constitutive model for a stress- and thermal-induced phase transition in a shape memory polymer *Smart Mater. Struct.* **23** 105019.

[2] L W Liu, Y J Liu, J S Leng and K T Lau 2011 Electromechanical stability of compressible dielectric elastomer actuators *Smart Mater. Struct.* **20** 115015.

[3] J S Leng, X Lan, Y J Liu and S Y Du 2011 Shape-memory polymers and their composites: Stimulus methods and applications *Prog. Mater. Sci.* **56** 1077-1135.

[4] Y Q Fu, H Du, W M Huang, S Zhang and M Hu 2004 TiNi-based thin films in MEMS applications: A review *Sens. Actuators A: Phys.* **112** 395-408.

[5] S Miyazaki, Y Q Fu and W M Huang 2009 *Thin Film Shape Memory Alloys: Fundamentals and biomedical Device Applications* (London: Cambridge University Press).

[6] Y Q Fu, S Sanjabi, Z H Barber, T W Clyne, W M Huang, M D Cai, J K Luo, A J Flewitt and W I Milne 2006 Evolution of surface morphology in TiNiCu shape memory thin films *Appl. Phys. Lett.* **89** 171922.

[7] Y Q Fu, H J Du and S Zhang 2003 TiNi SMA thin films: relationship among processing, stress evolution and transformation properties *Surf. Coat. Tech.* **167** 120–8.

[8] S Miyazaki and A Ishida 1999 Martensitic transformation and shape memory behavior in sputter-deposited TiNi-based thin films *Mater. Sci. Eng. A* **273-275** 106-13.

[9] H J Lee, H Ni, D T Wu and A G Ramirez 2005 Grain size estimations from the direct measurement of nucleation and growth *Appl. Phys. Lett.* **87** 124102.

[10] Y Liu and X Huang 2004 Substrate-induced stress and transformation characteristics of a deposited Ti-Ni-Cu thin films *Philos. Mag.* **84** 1919-36.

[11] T Habijan, R L De Miranda, C Zamponi, E Quandt, C Greulich, T A Schildhauer and M Köller 2012 The biocompatibility and mechanical properties of cylindrical NiTi thin films produced by magnetron sputtering *Mater. Sci. Eng. C* **32** 2523-28.

[12] K Otsuka and X Ren 2005 Physical metallurgy of Ti-Ni-based shape memory alloys *Prog. Mater. Sci.* **50** 511-678.

[13] T Duerig, A Pelton and D Stöckel 1999 An overview of nitinol medical applications *Mater. Sci. Eng. A* **273-275** 149-60.

[14] S A Shabalovskaya 2002 Surface, corrosion and biocompatibility aspects of nitinol as an implant material *Bio-Medical Materials and Eng.* **12** 69-109.

[15] S Shabalovskaya and J van Humbeeck 2009 *Biocompatibility of nitinol for biomedical applications, in: T. Yoneyama, S. Miyazaki (Eds.), Shape Memory Alloys for Biomedical Applications* (New York, CRC Press LLC) pp. 194-236.

[16] M J Wu, W M Huang, Y Q Fu, F Chollet, Y Y Hu and M Cai 2009 Reversible surface morphology in shape-memory alloy thin films *J. Appl. Phys.* **105** 033517.

[17] T Zhao, Y Li, Y Xia, S S Venkatraman, Y Xiang and X Zhao 2013 Formation of a nano-pattering NiTi surface with Ni-depleted superficial layer to promote corrosion resistance and endothelial cell-material interaction *J Mater. Sci.-Mater. Med.* **24** 105-14.

[18] T Zhao, Y Li, X Zhao, H Chen and T Zhang 2012 Ni ion release, osteoblasts-materials interactions and hemocompatibility of hafnium implanted NiTi alloy *J. Biomed. Mater. Res. B* **100** 646-59.

[19] T Zhao, R Yang, C Zhong, Y Li and Y Xiang 2011 Effective inhibition of nickel release by tantalum-implanted TiNi alloy and its cyto-compatibility evaluation in vitro *J. Mater. Sci.* **46** 2529–35.

[20] T Zhao, Y Li, Y Gao, Y Xiang, H Chen and T Zhang 2011 Hemocompatibility investigation of the NiTi alloy implanted with tantalum *J Mater. Sci.-Mater. Med.* **22** 2311-18.

[21] T. Zhao, Y. Li, Y. Xiang, X Zhao and T Zhang 2011 Surface characteristics, nano-indentation and corrosion behavior of Nb implanted NiTi alloy *Surf. Coat. Tech.* **205** 4404–10.

[22] M J Duarte, J Klemm, S O Klemm, K J J Mayrhofer, M Stratmann, S Borodin, A H Romero, M Madinehei, D Crespo, J Serrano, S S A Gerstl, P P Choi, D Raabe and F U Renner 2013 Element-resolved corrosion analysis of stainless-type glass-forming steels *Science* **341** 372-6.

[23] C C Shih, S J Lin, K H Chung, Y L Chen and Y Y Su 2000 Increased corrosion resistance of stent materials by converting current surface film of polycrystalline oxide into amorphous oxide *J. Biomed. Mater. Res*. **52** 323-32.

[24] T Waitz, K Tsuchiya, T Antretter and F D Fischer 2009 Phase transformations of nanocrystalline martensitic materials *MRS Bull.* **34** 814-21.

[25] E Saebnoori, T Shahrabi, S Sanjabi, M Ghaffari and Z H Barber 2015 Surface characteristics and electrochemical behaviour of sputter-deposited NiTi thin film *Philos. Mag.* **95** 1696-1716.

[26] V A Alves and C M A Brett 2002 Characterization of passive films formed on mild steel in bicarbonate solution by EIS *Electrochim. Acta* **47** 2081-91.

[27] B G Pound 2008 The electrochemical behavior of nitinol in simulated physiological solutions *J. Biomed. Mater. Res. A* **85** 1103-13.

[28] B G Pound 2010 Electrochemical behavior of cobalt-chromium alloys in a simulated physiological solution *J. Biomed. Mater. Res. A* **94** 93-102.

[29] ASTM Standard F 2129-08 2008 *Standard test method for conducting cyclic potentidynamic polarization measurements to determine the corrosion susceptibility of small implant devices* (West Conshohocken, Pennsylvania, ASTM International).

[30] W S Hwang, K J Kim and W C Seo 1994 *Pitting corrosion of NiTi shape memory alloy in deaerated chloride solution in: 3th International Corrosion Congress* (Houston, TX, NACE International) Paper No. 381.

[31] J L Gilbert 1998 Step-polarization impedance spectroscopy of implant alloys in physiologic solutions *J Biomed. Mater. Res.* **40** 233-43.

[32] D R Lide 1999 *Handbook of Chemistry and Physics, 80th ed*. (New York, CRC Press LLC).

[33] S Shabalovskaya, J Anderegg and J van Humbeeck 2008 Critical overview of nitinol surfaces and their modifications for medical applications *Acta Biomater*. **4** 447-67.

[34] J P Bearinger, C A Orme and J L Gilbert 2003 In situ imaging and impedance measurements of titanium surface using AFM and SPIS *Biomater*. **24** 1837-52.